



Garnet related lithium ion conductor processed by spark plasma sintering for all solid state batteries



Seung-Wook Baek*, Jae-Myung Lee, Tae Young Kim, Min-Sang Song, Youngsin Park

Energy Laboratory, Samsung Advanced Institute of Technology (SAIT), Samsung Electronics Co., Ltd., Giheung-gu, Yongin-si, 446-712 Gyeonggi-do, Republic of Korea

HIGHLIGHTS

- We reported the feasibility of assembling ASSB by spark plasma sintering process (SPS).
- Garnet related $\text{Li}_{7-x}\text{La}_3\text{Zr}_{1.5}\text{Ta}_{0.5}\text{O}_{12-d}$ showed superior structural stability than $\text{Li}_7\text{La}_3\text{Zr}_2\text{O}_{12}$ for SPS.
- SPS processed $\text{Li}_{7-x}\text{La}_3\text{Zr}_{1.5}\text{Ta}_{0.5}\text{O}_{12-d}$ showed the high ionic conductivity without structural decomposition.
- All solid battery assembled by SPS showed a surface capacity of 0.2 mAh cm^{-2} at 80°C .

ARTICLE INFO

Article history:

Received 30 August 2013

Received in revised form

17 October 2013

Accepted 21 October 2013

Available online 30 October 2013

Keywords:

Spark plasma sintering

Lithium ion conductor

Garnet

All solid state battery

ABSTRACT

Oxide-based all solid state battery (ASSB) systems require highly enhanced cell assemblies technology in the light of the sintering issue, although various inorganic-based lithium ion conductors have been proposed and attempted to be adopted in battery systems. Here, the compatibility of Li-La-(Zr-Ta)-O garnet related lithium ion conductors with ASSB systems processed by spark plasma sintering (SPS) is reported. Further, the challenges with respect to the material and processing are also discussed. $\text{Li}_{7-x}\text{La}_3\text{Zr}_{1.5}\text{Ta}_{0.5}\text{O}_{12-d}$ processed by SPS shows a high ionic conductivity of $1.35 \times 10^{-3} \text{ S cm}^{-1}$ and $1.23 \times 10^{-2} \text{ S cm}^{-1}$ at 25°C and 80°C , respectively. In addition, the material also shows good structural stability, which is a critical challenge encountered in garnet structured materials treated under severe SPS process conditions. An ASSB assembled by SPS using the $\text{Li}_4\text{Ti}_5\text{O}_{12}\text{-Li}_{7-x}\text{La}_3\text{Zr}_{1.5}\text{Ta}_{0.5}\text{O}_{12-d}$ composite electrode shows a surface capacity of 0.2 mAh cm^{-2} at 80°C . The battery shows a well-organized structure with a good lithium diffusion percolation path and the low solid contact resistance without any defects and undesirable reactions arising from the sintering method.

© 2013 Elsevier B.V. All rights reserved.

1. Introduction

The application of lithium ion batteries (LIBs) to electric vehicles (EV) and backup uninterruptible power supply (UPS) systems has been attempted widely throughout the globe. Technically, LIBs pose challenges in terms of scale-up and guaranteed safety. All solid state battery (ASSB) systems show significant promise of scale-up and ensure safety, unlike the presently used organic liquid and polymer-based LIBs. Oxide-based ASSB systems require highly enhanced cell assembly technologies because of the high interface resistance related to sintering, although these systems are electrochemically and chemically stable under severe cell operation

environments. Until recently, some approaches such as the thin film battery assembly, have been applied in the fabrication of small ASSB systems. However, the performance of commercially available batteries is yet to be achieved, although various oxide-based lithium ion conductors such as $(\text{Li},\text{La})\text{TiO}_3$, $(\text{Li},\text{La})\text{ZrO}_2$, and LiPON have been adopted in these battery systems [1,2].

Oxide-based ASSBs require the following.

- 1) A lithium ion conductor (electrolyte) with a conductivity of at least $10^{-4} \text{ S cm}^{-1}$ at room temperature
- 2) Redox stability of lithium (when lithium is used as the anode material)
- 3) A wide electrochemical stability window (when lithium metal anode and high voltage cathode material are required to obtain a large capacity)
- 4) Sinterability at low temperature to reduce the interface resistance

* Corresponding author. Tel.: +82 31 280 6987; fax: +82 31 280 9359.

E-mail addresses: baeksw77@gmail.com, swook.baek@samsung.com (S.-W. Baek).

- 5) Chemical non-reactivity between components to enhance the lithium ion transport
- 6) Stability of the crystal structure under high temperature heat treatment
- 7) Formation of a rigid and flexible battery body to obtain a large area cell

Several inorganic-based solid lithium conductors have been proposed for use in ASSBs as mentioned above. Li_3PO_4 is a well-known lithium conductor with a high electrochemical stability; however, it is seldom used as a solid electrolyte because of its low lithium conductivity [3]. Instead of Li_3PO_4 , nitrogen substituted LiPON has been used as a thin film electrolyte in thin film batteries [4–6]. However, LiPON shows a low ionic conductivity of $10^{-6} \text{ S cm}^{-1}$ at room temperature, which limits its wide application. Recently, several research groups have focused on the development of solid electrolytes with high lithium ionic conductivities. Perovskite structured crystalline $\text{Li}_{0.35}\text{La}_{0.55}\text{TiO}_3$ (LLT), garnet structured crystalline $\text{Li}_7\text{La}_3\text{Zr}_2\text{O}_{12}$ (LLZ), nasicon structured $\text{Li}_{1.4}\text{Al}_{0.4}\text{Ti}_{1.6}(\text{PO}_4)_3$ (LATP), $\text{Li}_{1.5}\text{Al}_{0.5}\text{Ge}_{1.5}(\text{PO}_4)_3$ (LAGP), superionic sulfide crystal $\text{Li}_2\text{S}-\text{P}_2\text{S}_5$, and the newly developed superionic conductor $\text{Li}_{10}\text{GeP}_2\text{S}_{12}$ have been proposed to be used as the solid electrolytes [7–22]. All types of inorganic solid electrolytes, including the sulfide material, show extremely high interface resistances, although the sulfide material can be directly used as a solid electrolyte without any heat treatment like sintering because of its softness, which is different from ceramic or glass ceramic materials. In the case of LLT, electrolyte decomposition by Ti with a redox potential lower than 1.8 V vs. Li/Li^+ is a critical intrinsic problem. Garnet structured LLZ shows a high lithium ionic conductivity, which is greater than $10^{-4} \text{ S cm}^{-1}$ at room temperature, stable electrochemical properties, and low grain boundary resistance; however, it is unstable against moisture and shows crystalline instability. LLZ with a cubic structure generally shows high ionic conductivity; however, the material easily decomposes to the tetragonal phase or $\text{La}_2\text{Zr}_2\text{O}_7$ during high temperature heat treatment. From this processing view point, LLZ requires high sintering temperatures (above 1100°C) to achieve densification, which poses difficulties in the assembly of other electrode materials in terms of the formation of undesirable resistance layers by elemental diffusion and phase decomposition by lithium volatilization. Glass ceramics LAGP and LATP show high lithium ion conductivities ($>10^{-4} \text{ S cm}^{-1}$) and high sinterability at relatively low temperatures of around 800°C . These materials are also stable against moisture and can also be used as a separator in liquid electrolyte-based lithium-air batteries. However, configuration of the cell using these materials is still a challenge because of the electrolyte decomposition on contact with lithium metal and the high reactivity with electrode materials during heat treatment.

In ASSB research, thin film batteries are favored and their fabrication is based on thin film processing technologies like sputtering, low pressure chemical vapor deposition (LPCVD), pulsed laser deposition (PLD), and atomic layer deposition (ALD) [23,24]. Achieving high-energy capacity in this configuration is difficult, and the scale up potential by adopting a high throughput process is also limited, although the micro batteries show reliable battery behavior.

The configuration and fabrication of oxide-based ASSBs is technically challenging, specifically in the view of achieving performances of commercially available batteries because of the difficulties involved in ceramic processing. The low sinterability of the electrolyte and the electrode causes high interface resistance, and the volatilization of lithium causes the collapse of the crystal structure of the electrolyte during the high temperature sintering, resulting in a low lithium ion conductivity (of $<10^{-6} \text{ S cm}^{-1}$). Thus,

due to the limitations posed by the materials, ASSB fabrication is still considered as a technological obstacle. This is the reason for the increased focus on electrolyte materials in the recent reports on ASSBs, while very little progress is witnessed in developing full cell applications.

Ideally, the use of a low processing temperature without lithium volatilization, achievement of high interface adhesion induced by sintering, a low thermal mismatch between the battery components, and avoidance of cell fracture by shrinkage differences during cell fabrication are aimed for. ASSB fabrication methodologies can be categorized as those involving sintering and those that do not. Conventional ceramic processes such as powder compression, slurry casting, and tape casting are recognized as processes that involve sintering. These techniques usually require treatment at high temperatures to connect the particles or layers. During the use of these techniques, the collapse of the crystal structure by lithium volatilization and the decomposition of the material by any undesirable reactivity between the electrolyte and electrode are to be considered. Hence, an electrolyte with a thermally stable crystal structure and an electrolyte, which does not react with the electrode, are to be used in fabrication processes involving sintering. The processes that do not involve sintering may be considered to avoid the negative thermal effects. Besides thin film processing, various coating processes satisfying the cell energy capability and high throughput manufacturing requirements such as plasma spray, high velocity oxyfuel spraying (HVOF), cold spray, and aerosol deposition can also be used for the fabrication of ASSBs. Plasma spray and HVOF, which uses a high temperature flame, cannot be used directly in the present technology because the extremely high processing temperature can cause structural decomposition of the components. However, cold spray and aerosol deposition can be considered as potential ASSB fabrication processes. These fabrication processes require room temperature, and densified layers can be formed without structural decomposition of any material. However, these processes give rise to issues such as weak adhesion to the current collector, high grain boundary resistance, and lower ionic conductivity than the sintered body.

The formation of conduction pathways for the diffusion and migration depends on the sintering of particles in the case of fabrication of oxide-based ASSBs. It still shows a high interface resistance, although a room temperature coating process like the aerosol deposition process, which uses high impact energy, can be considered as a fabrication method without involving sintering. Among the various processes for ASSB fabrication, spark plasma sintering (SPS) offers several advantages such as the use of relatively low sintering temperatures, the use of a single step simple co-sintering protocol without thermal mismatch, and short processing time. In the SPS process, sintering temperatures as low as $100\text{--}300^\circ\text{C}$ can be used compared to the high temperatures used in conventional sintering processes, although the optimal processing temperature depends on the material composition and structural stability. The temperature range $800\text{--}1000^\circ\text{C}$ for heat treatment of oxide-based electrolytes and electrodes is a critical temperature range, which exerts a profound effect on the sinterability, structural stability, and undesirable reactivity. From this view point, lowering the heat treatment temperature through the use of advanced processing and developed materials is a significant challenge in the research and development of sintered ASSBs. SPS with short processing times and relatively low processing temperatures is one of the potential processes for ASSB fabrication.

In the present study, we have attempted to develop a solid electrolyte and an all solid state lithium rechargeable battery processed by SPS. This study focuses on characterization of the electrolyte subjected to SPS and the feasibility of ASSB assembly with the characterized electrolyte and $\text{Li}_4\text{Ti}_5\text{O}_{12}$ (LTO) electrodes.

Selection of materials based on various intrinsic requirements and encountered characteristics during processing should be carefully considered for cell assembly if the ASSB is fully processed under high temperature heat treatment inducing sintering as in the case of SPS. The application of LLZ as the electrolyte in an ASSB using conventional sintering process is not favored because of the low ionic conductivity from the instability of the crystal structure, and poor sinterability. Thus, to fully make use of the benefits of the garnet structured electrolyte and SPS, a more durable electrolyte material with structural stability and good sinterability under severe processing environments and at relatively low heat treatment temperatures is required. $\text{Li}_{7-x}\text{La}_3\text{Zr}_{1.5}\text{Ta}_{0.5}\text{O}_{12-d}$ (LLZT) is an electrolyte material that is applicable for SPS, which is designed and characterized for the assembly of ASSBs. In this research study, the stability of the crystal structure, ionic conductivity, and sinterability of LLZ and LLZT synthesized by a solid-state process have been analyzed under SPS conditions. The assembly of ASSB supported by designed SPS process has been accomplished. The characteristics of the ASSB and challenges encountered in its assembly are also discussed.

2. Experimental

Garnet structured polycrystalline cubic LLZ and LLZT were synthesized by a solid-state reaction. The starting materials were $\text{LiOH} \cdot \text{H}_2\text{O}$, La_2O_3 , ZrO_2 , and Ta_2O_5 (Aldrich). The precursors were weighed and ball milled with isopropyl alcohol (Aldrich) at 200 rpm for 12 h. Excess lithium (20 wt.%) was added to compensate lithium loss by volatilization during high temperature calcination. After drying in a convection oven, the uniformly mixed LLZ powder was calcined at 900 °C for 6 h. The calcined powder was reground and dried under the same conditions and heated at 1100 °C for 12 h in a second cycle of calcination. The powder was reground, pelletized, and sintered at 1130 °C and 1230 °C for 36 h to obtain the cubic structured garnet electrolyte. The two-step calcination process was applied for the LLZT synthesis. The mixed LLZT precursors were calcined at 1000 °C for 12 h during the first calcination step. Then, the powder was reground and calcined at 1200 °C for 20 h during the second calcination step. Finally, the calcined LLZ and LLZT powders were reground and sieved to obtain uniform particles. LTO (Umicore) was used as the electrode material along with the LLZT electrolyte to assemble the all-solid lithium battery. Ag powder (Heesung Metal Ltd.) with a diameter of 1 μm (d50) was used as the electron conducting material and LLZT was added to relax the thermal mismatch and reduce the interfacial

resistance between the electrode and electrolyte during SPS. The LTO (30 wt.%)–Ag (30 wt.%)–LLZT (40 wt.%) mixture (LTO–Ag–LLZT 334) was ball milled for 24 h.

An SPS machine (Dr. Sinter SPS-511S, Sumitomo coal mining Co. Ltd.) and a carbon mold were used to prepare the samples. The schematic of the SPS process and the sintering mechanism is shown in Fig. 1. SPS uses high ampere DC pulse current to generate a spark plasma between the particles, as shown in Fig. 1(a). Uniaxial compression is applied and the process is carried out under vacuum or inert gas atmosphere. Discharge is generated at the particle contact point during the SPS process. Heat and high pressure are concentrated in this small contact area, and joule heating is generated by the electrical current (Fig. 1(b)). Necking of the particles begins, and sintering and densification proceed to occur. The details of the SPS processing sequences are introduced in Fig. 2. The prepared materials were packed into the carbon mold and uniaxial precompression was carried out to increase the packing density before SPS. A carbon punch with a diameter of 10 mm was used and a static pressure of 50 MPa was applied during the process. The samples were held for 10 min in the temperature range 300–1000 °C under vacuum. The voltage and current used in the process were controlled under the automatic operation mode. The temperature increase rate was set to 50 °C min^{-1} . Alternate layers of the LTO–Ag–LLZT 334 electrode and the LLZT electrolyte calcined at 1000 °C were placed in a carbon mold. The LTO–Ag–LLZT 334/LLZT half-cell processed by SPS was assembled with lithium on a hot plate to configure the solid battery.

X-ray diffraction (XRD, PANalytical, Almelo) and scanning electron microscopy (SEM, Hitachi, S4800) were carried out to verify the crystal structure and the microstructure of the electrolyte, respectively. The concentration of the elements was determined by inductively coupled plasma atomic emission spectroscopy (ICP–AES) carried out on a sequential spectrometer (Shimadzu ICPS-8100) to verify the stability of the elements after SPS. The four probe method was used to measure the electrochemical AC impedance. Measurements were carried out in the range –10 °C to 80 °C in a vacuum-sealed pouch on an electrochemical interface/impedance gain-phase analyzer (Solartron 1287/Solartron 1260). The frequency ranged from 1×10^6 to 1×10^{-1} Hz and the applied voltage amplitude was 20 mV under open circuit voltage (OCV). The Solartron analytical 1400 & 1470E Cell Test System was used to investigate the charge–discharge battery characteristics. The ASSB battery was tested under 0.05C. An isothermal-isohumidity chamber (SU-261, ESPEC) was used to investigate the electrolyte conductivity and battery characteristics.

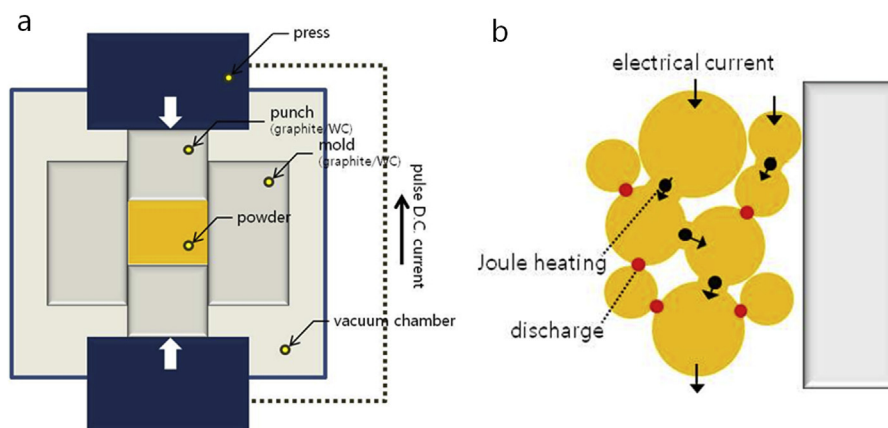


Fig. 1. Schematic of the SPS process. (a) Components of the SPS apparatus, (b) mechanism of the SPS.

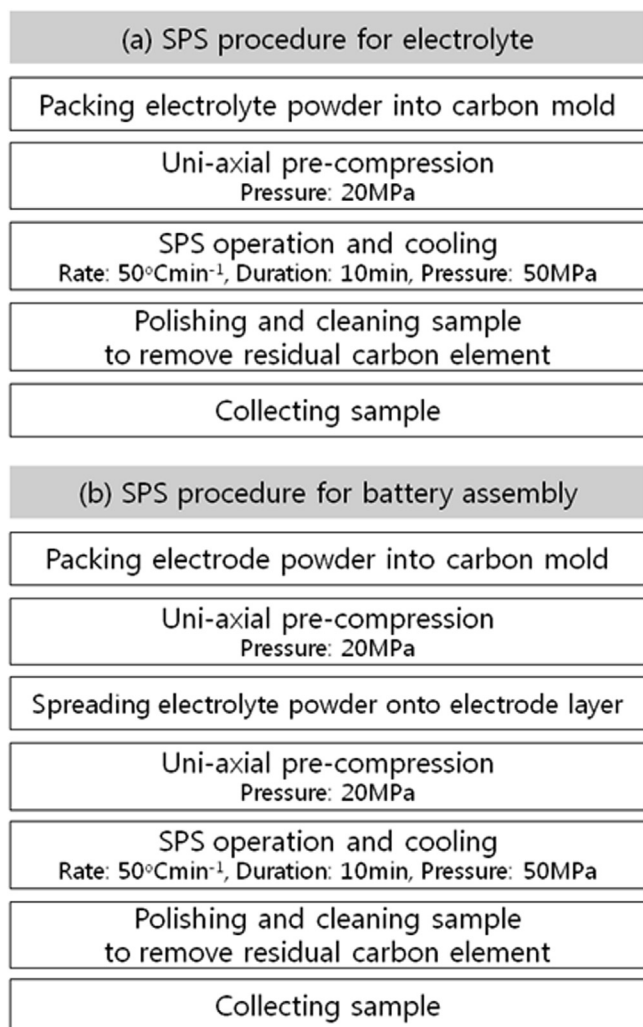


Fig. 2. SPS processing sequences.

3. Results & discussion

3.1. Structural stability

Appropriate calcination and sintering temperatures are required to obtain a stable cubic structure and to achieve a sintered body with a high ionic conductivity through the enhanced ionic conduction pathways, respectively, which are both necessary to assemble the ASSB. The XRD patterns of calcined/sintered LLZ samples (a-1–a-3) obtained with different heat treatment temperatures and SPS processed LLZ samples (b-1–b-4) obtained at 350–700 °C are shown in Fig. 3. In the case of LLZ, the tetragonal and cubic phases are identified, and it is known that LLZ with cubic phase shows high ionic conductivity. However, transformation of the crystal structure from the tetragonal phase to cubic phase begins at around 1100 °C. At 1130 °C, the tetragonal phase is still found to exist, although the cubic phase is obtained. The cubic phase formation is complete at 1230 °C. Consequently, a minimum temperature of 1230 °C seems to be required from the point of view of sinterability to achieve a sufficient intrinsic ionic path. However, 1200 °C is excessively high to assemble the ASSB because of the volatilization of lithium, the undesirable reactivity of the electrode material with the electrolyte, and the decomposition of the battery components. Hence, lowering the temperature to the value required for the cubic phase formation and sintering is essential.

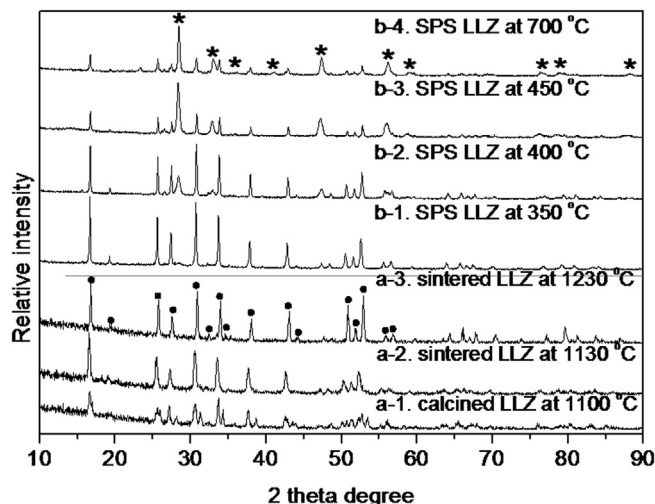


Fig. 3. XRD patterns of a-1. tetragonal LLZ calcined at 1100 °C, a-2. tetragonal/cubic LLZ sintered at 1130 °C and a-3. cubic LLZ sintered at 1230 °C, and b-1–b-4. LLZ subjected to SPS at 350–700 °C. ●: cubic phase index, *: $\text{La}_2\text{Zr}_2\text{O}_7$.

LLZ shows highly unstable structural properties under SPS operation, as shown in Fig. 3(b-1–b-4). The cubic structured garnet LLZ decomposes to mainly the thermodynamically stable $\text{La}_2\text{Zr}_2\text{O}_7$ at temperatures above 400 °C as a result of the extraction of Li_2O . The solidified Li_2O forms as a gray colored product, which is verified from the XRD patterns, as shown in Fig. 4, and Li_2O could be extracted from the mold because of the structural instability of LLZ. The weakly bonded lithium within the lattice of LLZ is converted to Li_2O under conditions of high pressure, high temperature, and an atmosphere with a low concentration of oxygen. However, sintering temperatures below 400 °C are too low to result in a sintered body, which can function as the electrolyte. The XRD patterns of the LLZT samples (a-1, a-2) obtained at different heat treatment temperatures and the patterns acquired from the SPS processed LLZT samples (b-1–b-6) at 700–1000 °C are shown in Fig. 5. The garnet structure with a clear cubic phase forms at 1000 °C without a tetragonal phase. LLZT requires lower heat treatment temperatures to achieve the garnet structure with cubic phase when compared to LLZ, although the sinterability of LLZT is almost similar to that of LLZ. LLZT still poses the issue of sinterability related to the cell

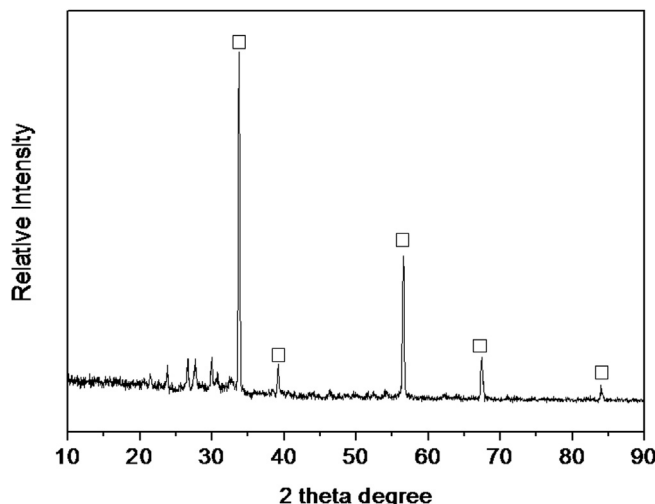


Fig. 4. XRD pattern of the residual LLZ phase obtained by SPS. □: Li_2O .

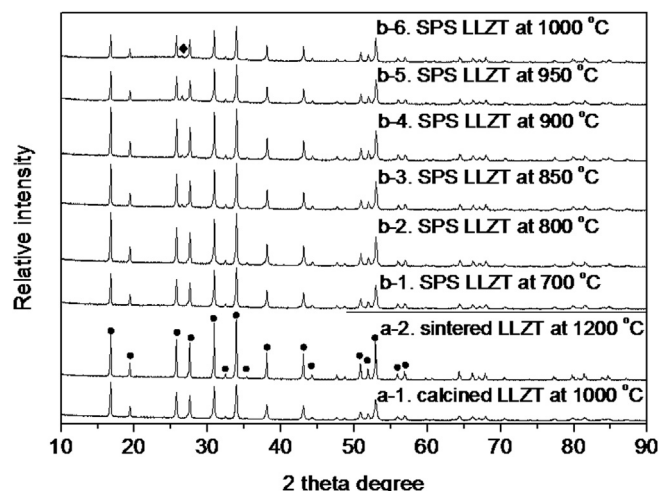


Fig. 5. XRD patterns of a-1. cubic LLZT sintered at 1000 °C and a-2. cubic LLZT sintered at 1200 °C, and b-1–b-6. LLZT subjected to SPS at the temperatures of 700–1000 °C. ●: cubic phase index, ◆: unknown peak.

assembly. As mentioned above, SPS involves pressurized sintering in vacuum. The structural stability of a material under these conditions should be considered prior to applying SPS to the cell assembly. Unlike LLZ, LLZT shows dramatically different structural stability, as shown in Fig. 5(b-1–b-6). LLZT maintains the cubic structure at 1000 °C, although an unknown peak is observed. Ta substitution in LLZ seems to have led to strong interactions between lithium and the surrounding atoms. Hence, based on the structural stability of LLZT, SPS may be advantageous in promoting sintering between the nanosized LLZT particles.

The molar concentration of the various elements, which is obtained from the ICP-AES analysis, is shown in Fig. 6. The initial lithium content of 7.06 mol in LLZ decreases with increase in the SPS temperature, as shown in Fig. 6(a). The lithium is extracted by the formation of Li_2O at around 400 °C and the cubic structured LLZ is converted into a mixed structure consisting of tetragonal LLZ and $\text{La}_2\text{Zr}_2\text{O}_7$, as mentioned Figs. 3 and 4. The second transformation to $\text{La}_2\text{Zr}_2\text{O}_7$ proceeds rapidly at 600 °C. The thermodynamically stable $\text{La}_2\text{Zr}_2\text{O}_7$ structure does not possess any ionic conductivity. Hence, the garnet structured cubic phase LLZ cannot be used as the lithium ion conducting electrolyte in conjunction with SPS because of its instability. However, lithium within the Ta-doped LLZT structure seems to have occupied stable lattice positions and the molar concentration of the elements remains unchanged despite treating the sample at a high temperature of 1000 °C (Fig. 6(b)).

3.2. Ionic conductivity

The Arrhenius plot of the LLZ sintered electrolytes with the tetragonal/cubic mixed phase and the single cubic phase is shown in Fig. 7. Both samples show ionic conductivities $>10^{-4} \text{ S cm}^{-1}$ and an activation energy of 0.36–0.38 eV. LLZ sintered at 1230 °C shows a higher ionic conductivity because of the formation of better lithium transportation pathways originating from the low grain boundary resistance caused by the high heat treatment temperature. SPS processed LLZT shows an activation energy of 0.39–0.40 eV, as shown in Fig. 8. The substitution of the Zr^{4+} sites with Ta^{5+} of a smaller ionic radius (of 78 pm) leads to a decrease in the lattice parameter and a decrease in the lithium concentration. The migration barrier for mobile lithium ions is higher, resulting in a higher activation energy [25,26].

3.3. Sinterability

LLZ sintered at 1230 °C does not possess a fully densified microstructure, as shown in Fig. 9(a) despite its high ionic conductivity of $1.68 \times 10^{-4} \text{ S cm}^{-1}$. The closed pores of the electrolyte after the sufficient necking driven by sintering do not affect the ionic conductivity; however, the insufficient sintering process results in the formation of open pores, which leads to decreased conductivity. The closed pores and the open pores are mixed, and the necking between particles is insufficient. These microstructural issues are strongly related to the high grain boundary resistance and the weak mechanical strength, which causes the occurrence and propagation of cracks that originate from the non-uniform structural density. The sinterability of LLZT sintered at 1200 °C is not any better than that of LLZ, as shown in Fig. 9(b), although the cubic phase is formed at relatively low temperatures. Ta substitution in LLZ does not affect the sinterability. The sintered LLZ and LLZT samples show non-uniform density over the entire structure, which originates from the non-uniformity of elemental concentration in the materials.

Densification by SPS differs from densification resulting from general heat treatment. Joule heating at particle contact points caused by high current flow generates an arc. It is to be noted that conduction through LLZT, which is an insulating material, can be accomplished by discharging at the particle contact points with high resistance. The heating begins at the entire contact spot and propagates, which results in local melting. Unfortunately, the crystal structure of LLZ collapses during SPS because of the high energy directly loaded into material, although densification rapidly progresses within a very short time of 10 min at temperatures lower than that required for general sintering. The cross sectional image of the LLZT samples subjected to SPS at different

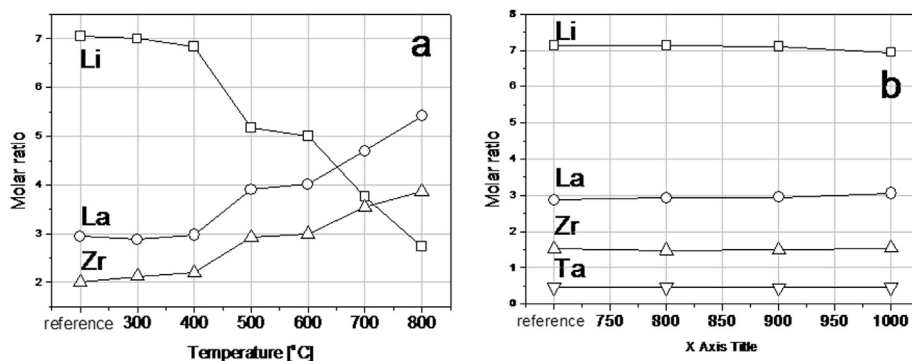


Fig. 6. ICP-AES analysis of (a) LLZ and (b) LLZT subjected to SPS at various temperatures. SPS duration: 10 min.

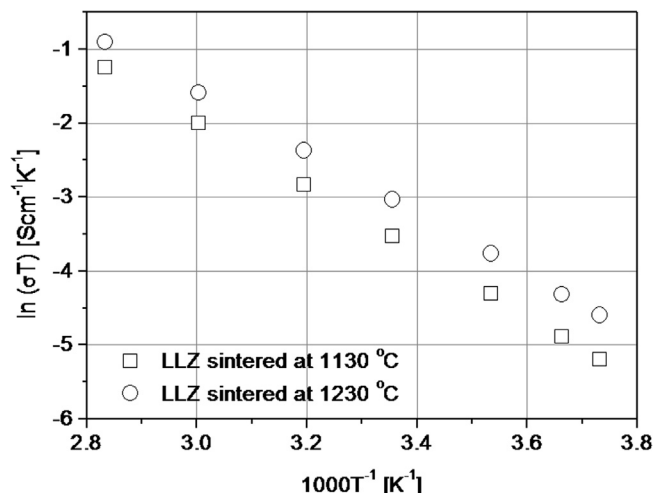


Fig. 7. Arrhenius plot for sintered LLZ.

temperatures is shown in Fig. 10. The microstructure is reorganized with the liquid phase sintering beginning at 700 °C. Most of the particles are connected, and a fully densified structure is obtained finally. Above 700 °C, local melting by the arc is accelerated and propagated. The sintering mechanism by SPS is entirely different from that of the conventional sintering method, as shown in Figs. 9

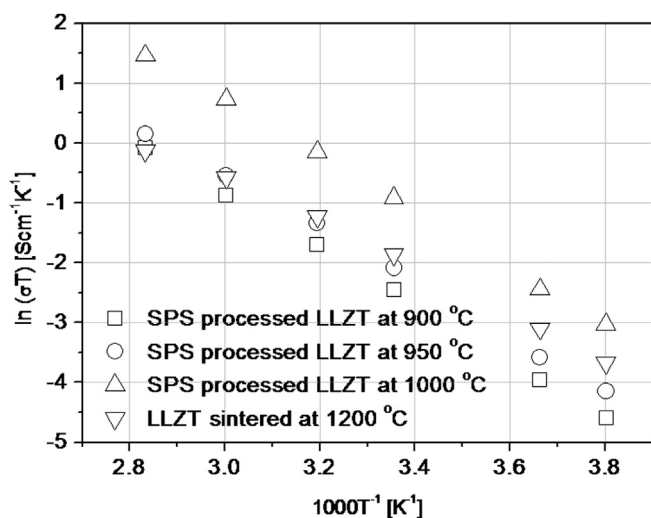


Fig. 8. Arrhenius plot for sintered LLZT and SPS-processed LLZT.

and 10. In the case of LLZT, which exhibits a high structural stability against an external energy source like high current flow during SPS, the SPS processing temperature can be lowered to obtain a densified durable electrolyte with a high ionic conductivity.

Table 1 summarizes the results obtained for the LLZ and LLZT garnet systems. From Table 1 and Fig. 6, it can be seen that the lithium content in the LLZT garnet system is maintained and the lithium is found to be contained within the lattice structure until 1000 °C. Other elements also exhibit the same tendency. A small amount of lithium is extracted and volatilized from the lattice at 1000 °C and simultaneously, the ratio of La and Zr is slightly changed. In the case of LLZT, the ionic conductivity increases with an increase in the duration and temperature of the SPS process. The ionic conductivities at room temperature and 80 °C are $1.35 \times 10^{-3} \text{ S cm}^{-1}$ and $1.23 \times 10^{-2} \text{ S cm}^{-1}$, respectively. The high conductivities originate from the formation of a highly densified electrolyte structure, without lattice decomposition.

The molar ratio of lithium in the LLZT sample sintered by conventional sintering is 7.13 and the ionic conductivity is $5.22 \times 10^{-4} \text{ S cm}^{-1}$. The ionic conductivity of LLZT subjected to SPS is, however, higher than that of the LLZT samples subjected to conventional sintering, although the molar ratio of lithium in the former is 6.87, which is less than 7.13. The ionic conductivity of the sintered electrolyte is mainly related to the intrinsic lattice properties including the lithium molar ratio and the extrinsic ion transport path formation and the grain boundary resistance. From the point of view of intrinsic lattice properties, the decrease of lithium content below 7.0 leads to an increase in the ionic conductivity, and it is known that the highest ionic conductivity is shown when the lithium content is around 6.5, which gives rise to short-range ordering [26,27]. LLZT shows reliable ionic conductivity at a wide range of lithium contents, although the lithium content is above 7.0.

3.4. Battery assembly by SPS

Oxide-based all-solid lithium batteries consisting of garnet structured electrolyte are yet to be reported. The ASSB technology is yet to see much progress because of the issue encountered with the decomposition of the electrolyte material by lithium volatilization caused by the high heat treatment temperature. In this paper, we have attempted to show the feasibility of fabricating an all-solid battery with a perfect solid interface. The results of the energy dispersive X-ray (EDX) analysis of the LTO-Ag-LLZT 334/LLZT half-cell processed by SPS at 900 °C are shown in Fig. 11. The electrode and electrolyte do not show layer delamination. The microstructure formation is investigated, as shown in Figs. 12 and 13. LTO and LLZT are connected by SPS. The highly networked LLZT present over the entire cell imparts mechanical strength to the cell and the

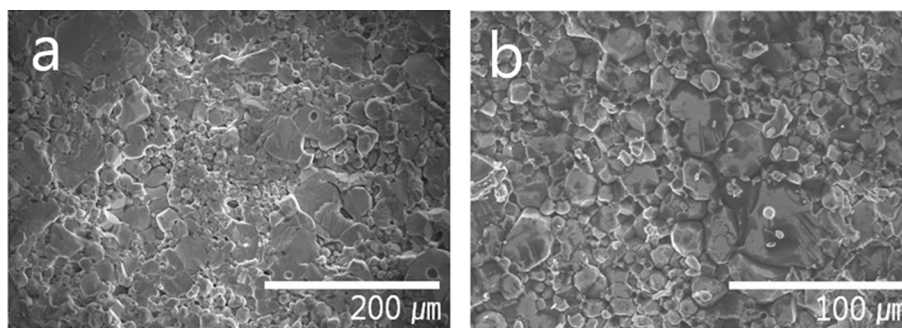


Fig. 9. Microstructures of (a) LLZ sintered at 1230 °C and (b) LLZT sintered at 1200 °C.

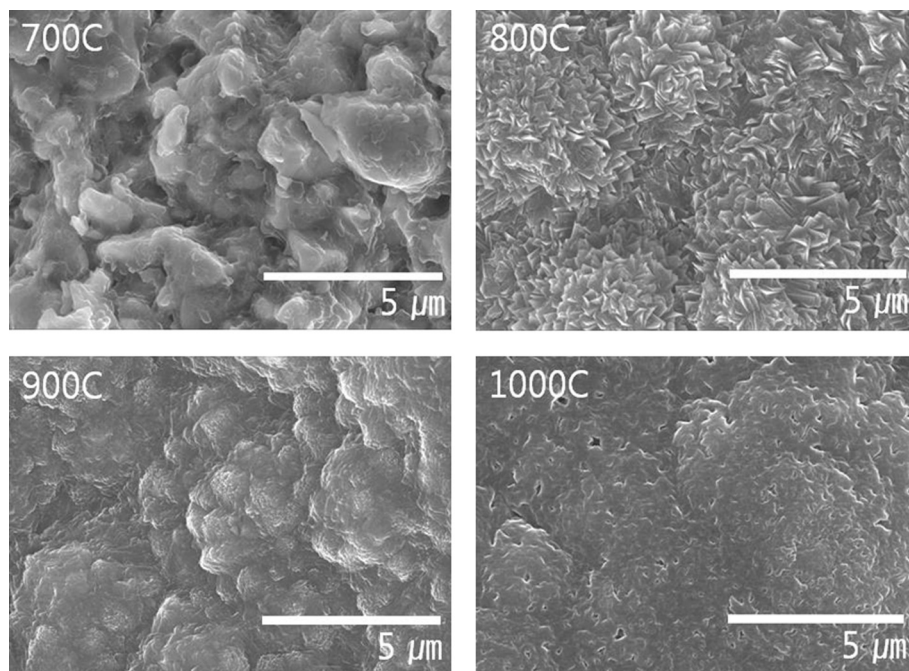


Fig. 10. Microstructures of LLZT samples subjected to SPS at different temperatures. SPS duration: 10 min.

largely extended interfaces with a low interfacial resistance between LTO and LLZT improve the electrochemical performance of the battery. The interface between the electrolyte and the electrode is well organized and it is difficult to distinguish the interface and the grain boundaries. The sintering temperature of the battery body is lowered below 1000 °C, and a single step co-sintering of the electrolyte and the electrode can be applied without defects related to thermal mismatch.

The uniform formation of electron conducting pathways in the electrode is shown in Fig. 13. Ag, the conducting material, and LTO, the electrode material, are well dispersed. Ag can supply sufficient electron conducting pathways with the percolation network. LTO-Ag-LLZT 334/LLZT half-cell processed by SPS is assembled with metallic lithium to configure the ASSB. The total cell resistance is measured at 80 °C under OCV, as shown in Fig. 14. The overall areal specific resistance is 400 $\Omega \text{ cm}^2$. A large portion of the resistance originates from the interface resistance. The formation of an oxide layer over the surface of the lithium metal is one of the causes of interface resistance; however, in the present research, the humidity and the temperature are controlled, resulting in the elimination of this factor. The interface resistance may also originate from the slower kinetics of the solid–solid interface when compared to that of the liquid electrolyte system, although a well-connected structure could be organized through the advanced sintering process.

The galvanostatic performance of the ASSB is measured at 80 °C, as shown in Fig. 15. The charge–discharge (C–DC) current is applied at the rate of 0.05C, and the charging cut-off potential is 2.5 V. The ASSB assembled using the LTO-Ag-LLZT composite electrode processed by SPS shows a surface capacity of 0.2 mAh cm^{-2} at 80 °C.

3.5. SPS profile analysis

The real time variations in the selected samples according to increase in temperature are monitored in terms of the dimensional change of the cells and the vacuum level change in the SPS chamber, as shown in Fig. 16. The sintering behavior and phase

separation behavior including the formation of Li_2O can be verified from the dimensional change, and the volatilization of lithium can be detected through the variation in the vacuum. In the case of LLZ, a large dimensional change is observed at the temperature range 200–500 °C. Further, the vacuum level fluctuates with a large variation, as shown in Fig. 16(a). The low temperature phase transition and thermal evolution through the volatilization of lithium, resulting in the formation of Li_2O are considered to occur. The phase separation to $\text{La}_2\text{Zr}_2\text{O}_7$ and Li_2O occurs at around 200–300 °C. These results match well with the thermal instability of the LLZ crystal structure, which is illustrated in Figs. 3, 4 and 6. In this temperature range, LLZT shows stable dimensions over the entire temperature range when compared to LLZ (Fig. 16(b)), although a small change in the vacuum level is observed at around 400 °C. Sintering of LLZ and LLZT begins at 670 °C and 620 °C, respectively, which is verified from the displacement information. Then, sintering gradually progresses with the increase in temperature. To investigate the behavior of the assembled ASSB (LTO-Ag-LLZT 334/LLZT half-cell), the behavior of LTO is also monitored with the same parameters. As expected, LTO shows the highly stable crystal structure, although any other variation is not observed, as shown in Fig. 16(d). Sintering begins at 680 °C under SPS operation and progresses relatively more rapidly when compared with the sintering of LLZT. From the view point of sintering characteristics, LLZT and LTO show compatibility at a similar temperature range. This compatibility of the sintering temperature is significant with respect to the well-established ASSB design of effectively achieving a sintered body without thermal mismatch.

In the present research study, the designed ASSB with a sintering point of 750 °C shows a stable thermal behavior based on the characteristics of LLZT and LTO, as shown in Fig. 16(c). The differences in the initial sintering temperature (620 °C, 680 °C, and 750 °C for LLZT, LTO, and ASSB, respectively) originate from the differences in the current flow paths in the inner structure for the sintering body. The structure of the ASSB consists of the multilayer electrolyte/electrode with interfaces and contains the composite electrode with different particle sizes and morphologies. The

Table 1

Summary of the results obtained for LLZ and LLZT.

Material & process	Temp. [°C]	Composition from ICP-AES	Crystal structure	Conductivity at 25 °C [S cm^{-1}]	Conductivity at 80 °C [S cm^{-1}]	Activation energy [eV]
Sintered LLZ	1130	$\text{Li}_{6.48}\text{La}_{3.32}\text{Zr}_{2.20}\text{O}_{12}$	Cubic/tetragonal	1.01×10^{-4}	—	0.38
	1230	$\text{Li}_{6.85}\text{La}_{3.09}\text{Zr}_{2.07}\text{O}_{12}$	Cubic	1.68×10^{-4}	—	0.36
SPS processed LLZ	300	$\text{Li}_{7.00}\text{La}_{2.88}\text{Zr}_{2.12}\text{O}_{12-d}$	$\text{La}_2\text{Zr}_2\text{O}_7$	—	—	—
	400	$\text{Li}_{6.84}\text{La}_{2.97}\text{Zr}_{2.19}\text{O}_{12-d}$	$\text{La}_2\text{Zr}_2\text{O}_7$	—	—	—
	500	$\text{Li}_{5.17}\text{La}_{3.91}\text{Zr}_{2.92}\text{O}_{12-d}$	$\text{La}_2\text{Zr}_2\text{O}_7$	—	—	—
	600	$\text{Li}_{5.00}\text{La}_{4.01}\text{Zr}_{2.99}\text{O}_{12-d}$	$\text{La}_2\text{Zr}_2\text{O}_7$	—	—	—
	700	$\text{Li}_{3.76}\text{La}_{4.70}\text{Zr}_{3.54}\text{O}_{12-d}$	$\text{La}_2\text{Zr}_2\text{O}_7$	—	—	—
	800	$\text{Li}_{2.73}\text{La}_{5.41}\text{Zr}_{3.86}\text{O}_{12-d}$	$\text{La}_2\text{Zr}_2\text{O}_7$	—	—	—
Sintered LLZT	1200	$\text{Li}_{7.13}\text{La}_{2.87}\text{Zr}_{1.52}\text{Ta}_{0.47}\text{O}_{12-d}$	Cubic	5.22×10^{-4}	2.50×10^{-3}	0.32
SPS processed LLZT	800	$\text{Li}_{7.13}\text{La}_{2.93}\text{Zr}_{1.48}\text{Ta}_{0.47}\text{O}_{12-d}$	Cubic	1.00×10^{-4}	—	—
	850	$\text{Li}_{7.11}\text{La}_{2.95}\text{Zr}_{1.49}\text{Ta}_{0.46}\text{O}_{12-d}$	Cubic	1.08×10^{-4}	—	—
	900	$\text{Li}_{7.07}\text{La}_{2.87}\text{Zr}_{1.53}\text{Ta}_{0.54}\text{O}_{12-d}$	Cubic	2.90×10^{-4}	2.61×10^{-3}	0.40
	950	$\text{Li}_{6.94}\text{La}_{3.05}\text{Zr}_{1.54}\text{Ta}_{0.47}\text{O}_{12-d}$	Cubic	4.18×10^{-4}	3.30×10^{-3}	0.39
	1000	$\text{Li}_{6.87}\text{La}_{3.07}\text{Zr}_{1.60}\text{Ta}_{0.56}\text{O}_{12-d}$	Cubic	1.35×10^{-3}	1.23×10^{-2}	0.41

complex structure of the ASSB leads to changes in the current flow paths and the joule heating points, resulting in changes in the sintering behavior. The process parameters for sintering of the multilayered structure and composite material needs to be studied in detail based on the SPS mechanism in future studies. Optimized SPS process parameters can be expected to accomplish enhanced ASSB performances.

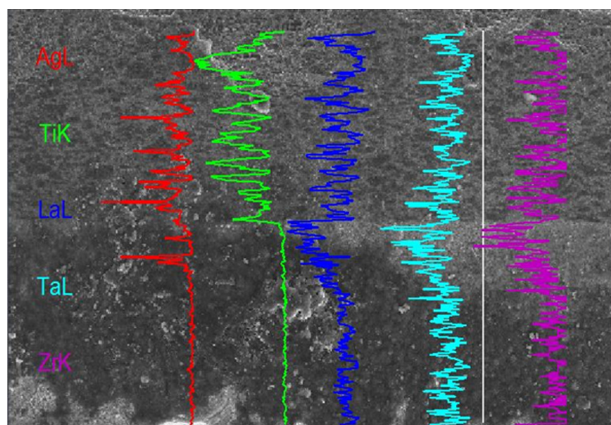


Fig. 11. EDX analysis of the assembled LTO-Ag-LLZT 334/LLZT half-cell subjected to SPS. *SPS conditions: maximum temperature; 900 °C, duration: 10 min, rate: 50 °C min⁻¹, applied static pressure: 50 MPa.

3.6. Progress and challenges in ASSB research

Recent research on ASSBs has mainly focused on the study of electrolytes with high ionic conductivities. The safety and high volumetric energy density of ASSBs offer significant advantages over conventional LIBs. However, the study of battery assembly and configuration has made limited advances because of the high technical process barrier. Cell configurations based on superionic sulfide crystal electrolytes, which show low contact resistance and solubility related processing issues and those based on the glass ceramic nasicon system, which require a relatively low heat treatment temperature, have been attempted. However, several problems such as reactivity with lithium, undesirable reactivity with electrode materials, and instability against moisture exist. Battery assemblies using garnet structured electrolyte materials like LLZ, which are stable against metallic lithium, are limited because of unstable crystal structures and the requirement of high heat treatment temperatures.

In the present study, we have demonstrated that the partially Ta substituted LLZT shows a highly stable crystal structure under high-temperature heat treatment conditions. Further, we have shown that the fabrication of the LLZT electrolyte with a high ionic conductivity and the assembly of a battery using LLZT using heat treatment processing at relatively low temperatures could be accomplished by SPS. As previously mentioned, the performance of the ASSB depends on the formation of conductive paths for the lithium ions and electrons. The next key issue is the interface control. Hence to enhance the battery performances, the following issues need to be addressed in future studies i.e., the selection and

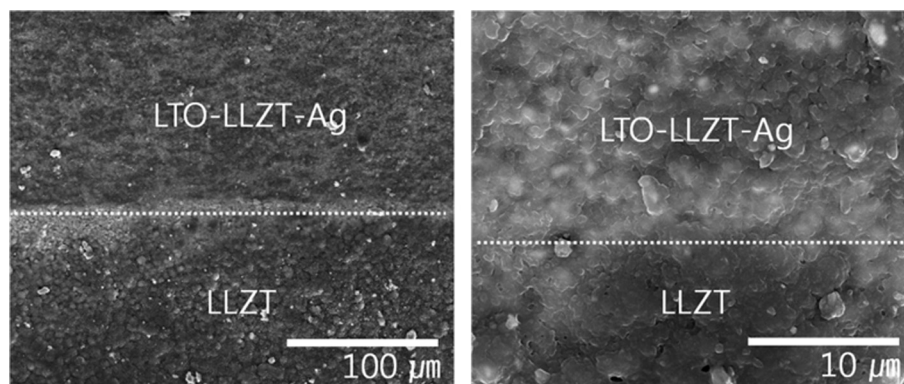


Fig. 12. Microstructures of the assembled LTO-Ag-LLZT 334/LLZT half-cell subjected to SPS. *SPS conditions; maximum temperature: 900 °C, duration: 10 min, rate: 50 °C min⁻¹, applied static pressure: 50 MPa.

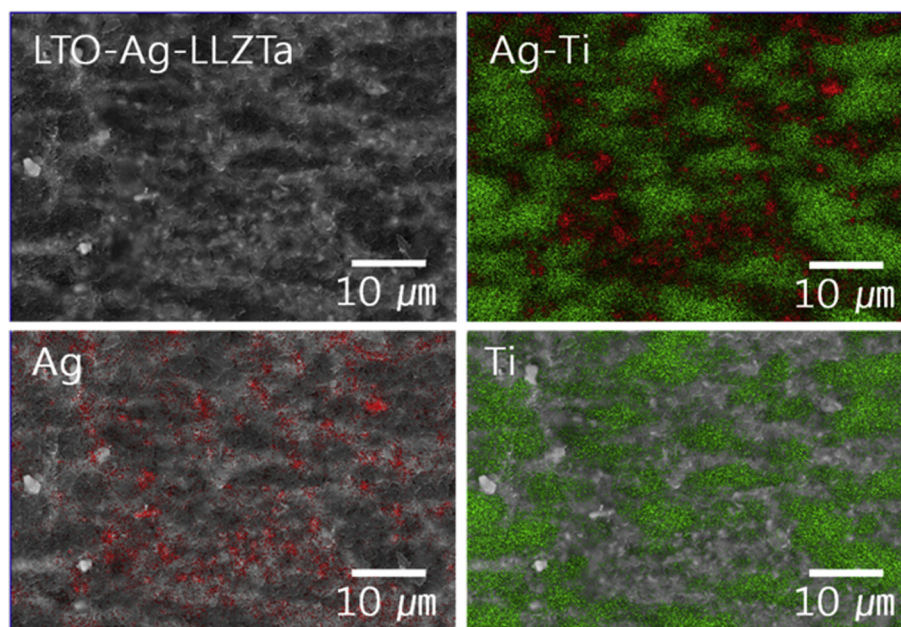


Fig. 13. EDX mapping of the electrode side of the assembled LTO-Ag-LLZT 334/LLZT half-cell subjected to SPS. *SPS conditions; maximum temperature: 900 °C, duration: 10 min, rate: 50 °C min⁻¹, applied static pressure: 50 MPa.

the use of 1) appropriate conducting materials, 2) optimal composite electrode compositions, 3) heat treatment temperatures based on the reactivity between the electrode and the electrolyte, 4) fine-tuned SPS conditions, 5) materials related to the enhancement of sinterability (e.g. element substituted materials or sintering aids). In addition, the formation of thinner electrolyte layers with SPS process also needs to be accomplished. Achieving optimized electrodes along with electrolyte formation with high ionic conductivities is necessary to obtain ASSBs with high performance. The formation of percolation paths for the conduction of lithium ions and electrons through the well-dispersed and controlled composite ratio (conducting material, electrode and electrolyte) needs to be achieved. Further, the use of similar sintering temperatures for the selected electrode and electrolyte materials is required to avoid any undesired reactions and thermal mismatch.

Most of the electrochemical reaction sites of the ASSB can be expected to be localized at the interface between the electrolyte and the electrode because of the slow kinetics at the solid–solid contact. Thus, designing of ASSBs with thin electrodes based on the calculated cell capacity is required to minimize the large over-potential caused by the long transport paths of ions and multiple grain boundaries.

4. Conclusions

In this paper, the feasibility of assembling ASSBs based on an oxide material is demonstrated. First, the garnet structured LLZ and partially Ta-substituted LLZT, which is stable toward metallic lithium and compatible with SPS processing, are characterized for

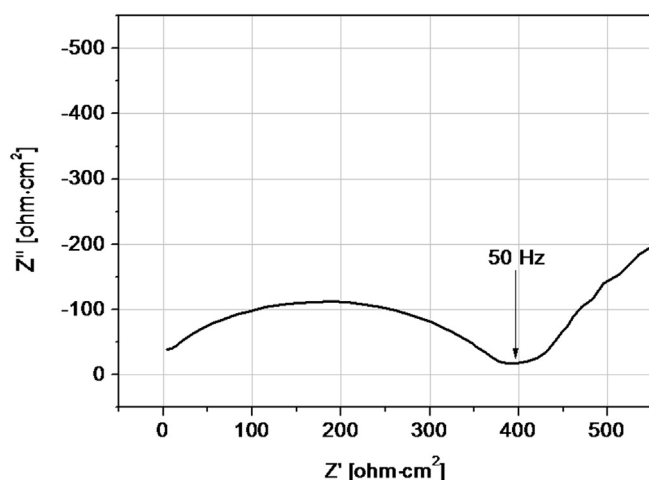


Fig. 14. Impedance characteristics of the ASSB assembled with SPS-processed LTO-Ag-LLZT 334/LLZT and metallic lithium. *SPS conditions; maximum temperature: 900 °C, duration: 10 min, rate: 50 °C min⁻¹, applied static pressure: 50 MPa. *Measurement conditions: 80 °C, OCV.

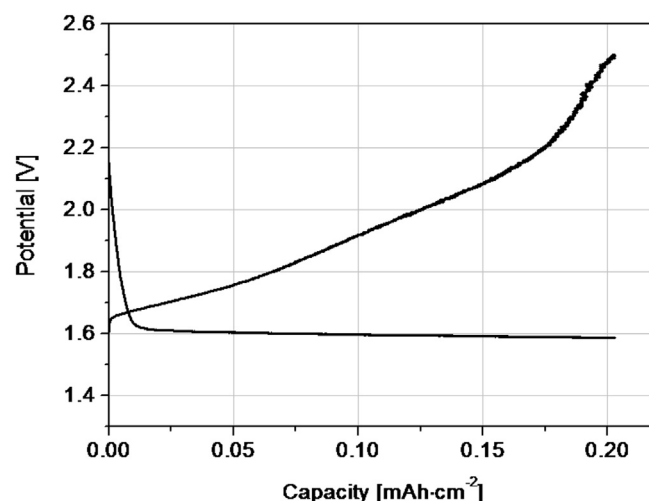


Fig. 15. Charge–discharge (C–DC) characteristics of the ASSB assembled with SPS processed LTO-Ag-LLZT 334/LLZT and metallic lithium. *SPS conditions; maximum temperature: 900 °C, duration: 10 min, rate: 50 °C min⁻¹, applied static pressure: 50 MPa. *C–DC condition: 0.05C, 80 °C.

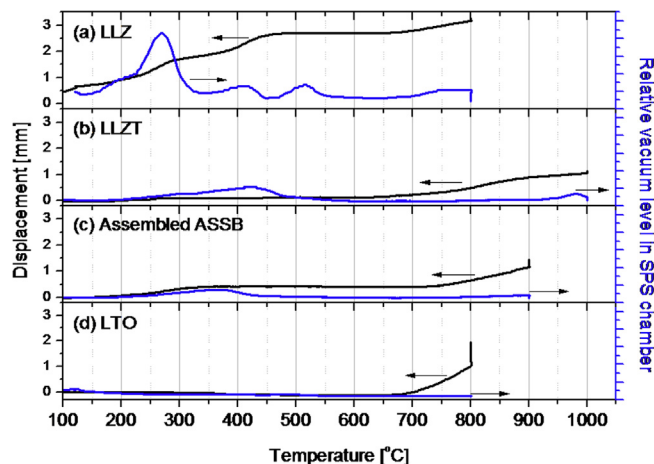


Fig. 16. Real time variations observed for (a) LLZ, (b) LLZT, (c) ASSB consisting of LTO-Ag-LLZT 334/LLZT, and (d) LTO subjected to SPS in terms of the dimensional change (displacement) and relative vacuum level in the SPS chamber, *SPS conditions; maximum temperature duration: 10 min, rate: 50 °C min⁻¹, applied static pressure: 50 MPa.

their application as electrolytes. Then, the LLZT electrolyte and LTO-Ag-LLZT 334 composite electrode are assembled under specified SPS conditions and evaluated with lithium metal electrode. Finally, several requirements and the key success factors for the development of ASSBs processed by SPS are discussed with respect to the improvement of cell performance.

LLZT shows a higher structural stability than LLZ when subjected to SPS. LLZT processed by SPS shows high ionic conductivities of $1.35 \times 10^{-3} \text{ S cm}^{-1}$ and $1.23 \times 10^{-2} \text{ S cm}^{-1}$ at 25 °C and 80 °C, respectively. The LTO-Ag-LLZT 334 composite electrode and the LLZT electrolyte are assembled with a well-organized and percolated microstructure using SPS. The ASSB assembled with metallic lithium shows a surface capacity of 0.2 mAh cm⁻² at 80 °C. The enhancement of battery performance and its scaling-up can be achieved in future if more specific processing conditions and material modifications are considered in the context of processing by SPS. The approach discussed and the results presented here are

expected to be recognized as a milestone in the development of post-LIB technologies that can supplant conventional LIBs.

References

- [1] P. Knauth, *Solid State Ionics* 180 (2009) 911.
- [2] J.W. Fergus, *J. Power Sources* 195 (2010) 4554.
- [3] M. Nagai, T. Nishino, *Solid State Ionics* 70/71 (1994) 96.
- [4] Y. Kim, G.M. Veith, J. Nanda, R.R. Unocic, M. Chi, N.J. Dudney, *Electrochim. Acta* 56 (2011) 6573.
- [5] F. Xu, N.J. Dudney, G.M. Veith, Y. Kim, C. Erdonmez, W. Lai, Y.M. Chiang, *J. Mater. Res.* 25 (2010) 1507.
- [6] S.H. Jee, M.J. Lee, H.S. Ahn, D.J. Kim, J.W. Choi, S.J. Yoon, S.C. Nam, S.H. Kim, Y.S. Yoon, *Solid State Ionics* 181 (2010) 902.
- [7] M. Kotobuki, Y. Suzuki, K. Kanamura, Y. Sato, K. Yamamoto, T. Yoshida, *J. Power Sources* 196 (2011) 9815.
- [8] T. Okumura, K. Yokoo, T. Fukutsuka, Y. Uchimoto, M. Saito, K. Amezawa, *J. Power Sources* 189 (2009) 536.
- [9] A. Mei, X.L. Wang, J.L. Lan, Y.C. Feng, H.X. Geng, Y.H. Lin, C.W. Nan, *Electrochim. Acta* 55 (2010) 2958.
- [10] J. Awaka, N. Kijima, H. Hayakawa, J. Akimoto, *J. Solid State Chem.* 182 (2009) 2046.
- [11] M. Kotobuki, K. Kanamura, Y. Sato, T. Yoshida, *J. Power Sources* 196 (2011) 7750.
- [12] Y. Li, C.A. Wang, H. Xie, J. Cheng, J.B. Goodenough, *Electrochem. Commun.* 13 (2011) 1289.
- [13] M. Kotobuki, Y. Isshiki, H. Munakata, K. Kanamura, *Electrochim. Acta* 55 (2010) 6892.
- [14] Y.H. Rho, K. Kanamura, *J. Power Sources* 158 (2006) 1436.
- [15] C.R. Mariappan, C. Yada, F. Rosciano, B. Roling, *J. Power Sources* 196 (2011) 6456.
- [16] J.S. Thokchom, B. Kumar, *J. Power Sources* 195 (2010) 2870.
- [17] C.R. Mariappan, M. Gellert, C. Yada, F. Rosciano, B. Roling, *Electrochem. Commun.* 14 (2012) 25.
- [18] M. Kotobuki, K. Hoshina, K. Kanamura, *Solid State Ionics* 198 (2011) 22.
- [19] H. Kitaura, A. Hayashi, T. Ohtomo, S. Hama, M. Tatsumisago, *J. Mater. Chem.* 21 (2011) 118.
- [20] A. Hayashi, K. Minami, M. Tatsumisago, *J. Non-Cryst. Solids* 355 (2009) 1919.
- [21] H. Kitaura, A. Hayashi, K. Yadanaga, M. Tatsumisago, *J. Mater. Res.* 25 (2010) 1548.
- [22] N. Kamaya, K. Homma, Y. Yamakawa, M. Hirayama, R. Kanno, M. Yonemura, T. Kamiyama, Y. Kato, S. Hama, K. Kawamoto, A. Mitsui, *Nat. Mater.* 10 (2011) 682.
- [23] A. Eftekhari, *J. Power Sources* 132 (2004) 240.
- [24] L. Baggetto, J.F.M. Oudenhoven, T. Dongen, J.H. Klootwijk, M. Mulder, R.A.H. Niessen, M.H.J.M. Croon, P.H.L. Notten, *J. Power Sources* 189 (2009) 402.
- [25] H. Buschmann, S. Berendts, B. Mogwitz, J. Janek, *J. Power Sources* 206 (2012) 236.
- [26] X. Xu, M. Park, J. Lee, T. Kim, Y. Park, E. Ma, *Phys. Rev. B* 85 (2012) 052301.
- [27] H. Xie, J. Alonso, Y. Li, M. Fernandez-Diaz, J. Goodenough, *Chem. Mater.* 23 (2011) 3587.